Electrical Wind Force–Driven and Dislocation-Templated Amorphization in Phase-Change Nanowires

Sung-Wook Nam *et al.*

Science **336**, 1561 (2012);
DOI: 10.1126/science.1220119

agreement with the size of the estimated pseudofield (45 nm). The density-of-states peaks observed as weakly negative sloping lines in the gate maps (Fig. 3A) may be caused by localization in a spatially varying pseudofield (*6*, *7*, *10*), although a detailed model is currently not available. The variations in positive-slope bands (Fig. 3, B to D) are probably caused by minor deformations of the overall membrane shape affecting the size of the QD.

References and Notes

1. K. S. Novoselov *et al.*, *Proc. Natl. Acad. Sci. U.S.A.* **102**, 10451 (2005).
2. K. I. Bolotin *et al.*, *Solid State Commun.* **146**, 351 (2008).
3. M. M. Fogler, F. Guinea, M. I. Katsnelson, *Phys. Rev. Lett.* **101**, 226804 (2008).
4. F. Guinea, M. I. Katsnelson, A. K. Geim, *Nat. Phys.* **6**, 30 (2010).
5. N. Levy *et al.*, *Science* **329**, 544 (2010).
6. K.-J. Kim, Y. M. Blanter, K.-H. Ahn, *Phys. Rev. B* **84**, 081401 (2011).
7. G. M. M. Wakker, R. P. Tiwari, M. Blaauboer, *Phys. Rev. B* **84**, 195427 (2011).
8. F. Guinea, B. Horovitz, P. Le Doussal, *Phys. Rev. B* **77**, 205421 (2008).
9. F. Guinea, A. K. Geim, M. I. Katsnelson, K. S. Novoselov, *Phys. Rev. B* **81**, 035408 (2010).
10. T. O. Wehling, A. V. Balatsky, A. M. Tsvelik, M. I. Katsnelson, A. I. Lichtenstein, *Europhys. Lett.* **84**, 17003 (2008).
11. M. Gibertini, A. Tomadin, M. Polini, *Phys. Rev. B* **81**, 125437 (2010).
12. S. Jung *et al.*, *Nat. Phys.* **7**, 245 (2011).
13. A. Luican, G. Li, E. Y. Andrei, *Phys. Rev. B* **83**, 041405 (2011).
14. J. A. Stroscio, E. W. Hudson, S. R. Blankenship, R. J. Celotta, A. P. Fein, *Proc. SPIE* **4608**, 112 (2002).
15. G. M. Rutter *et al.*, *Nat. Phys.* **7**, 649 (2011).
16. D. L. Miller *et al.*, *Science* **324**, 924 (2009).
17. G. Li, A. Luican, E. Y. Andrei, *Phys. Rev. Lett.* **102**, 176804 (2009).
18. Additional supplementary text and data are available on *Science* Online.
19. B. J. LeRoy, J. Kong, V. K. Pahilwani, C. Dekker, S. G. Lemay, *Phys. Rev. B* **72**, 075413 (2005).
20. L. P. Kouwenhoven, D. G. Austing, S. Tarucha, *Rep. Prog. Phys.* **64**, 701 (2001).
21. We determined the 1 SD error estimates in the QD sizes by combining the 1 SD in the addition energy variation for the first and last set of energies in Fig. 3G, together with the 1 SD uncertainties in the measured slopes of the charging lines in the gate maps.
22. M. I. Katsnelson, K. S. Novoselov, A. K. Geim, *Nat. Phys.* **2**, 620 (2006).
23. J. Güttinger *et al.*, *Phys. Rev. Lett.* **103**, 046810 (2009).

Acknowledgments: We thank M. Stiles and S. Adam for valuable discussions and S. Blankenship and A. Band for technical assistance. The U.S. National Science Foundation is gratefully acknowledged via grants CMMI-1069076 and CMMI-1129826 (T.L. and S.Z.) and grant CMMI-0841840 (C.A.W. and S.D.S.).

Supplementary Materials

www.sciencemag.org/cgi/content/full/336/6088/1557/DC1
Supplementary Text
Figs. S1 to S13
References (*24*–*26*)

9 February 2012; accepted 30 April 2012
10.1126/science.1220335

Electrical Wind Force–Driven and Dislocation-Templated Amorphization in Phase-Change Nanowires

Sung-Wook Nam,[1]* Hee-Suk Chung,[1]* Yu Chieh Lo,[1,2] Liang Qi,[1,2] Ju Li,[1,2] Ye Lu,[3] A.T. Charlie Johnson,[1,3] Yeonwoong Jung,[1] Pavan Nukala,[1] Ritesh Agarwal[1]†

Phase-change materials undergo rapid and reversible crystalline-to-amorphous structural transformation and are being used for nonvolatile memory devices. However, the transformation mechanism remains poorly understood. We have studied the effect of electrical pulses on the crystalline-to-amorphous phase change in a single-crystalline $Ge_2Sb_2Te_5$ (GST) nanowire memory device by in situ transmission electron microscopy. We show that electrical pulses produce dislocations in crystalline GST, which become mobile and glide in the direction of hole-carrier motion. The continuous increase in the density of dislocations moving unidirectionally in the material leads to dislocation jamming, which eventually induces the crystalline-to-amorphous phase change with a sharp interface spanning the entire nanowire cross section. The dislocation-templated amorphization explains the large on/off resistance ratio of the device.

Chalcogenide-based phase-change memory (PCM) materials have been widely used for optical data storage and are now finding applications in electronic memory devices (*1*, *2*). In a nonvolatile PCM device, the difference in optical reflectivity or electrical resistance between amorphous and crystalline phases is used to store information. Memory switching is performed by applying optical (or electrical) pulses: short pulses with large amplitude to amorphize the material and long pulses with low amplitude for the crystallization process. It has been generally assumed that the large amplitude of the pulse melts the material, and its short duration locks the atoms in their disordered positions owing to rapid quenching. The understanding of the effects of electric field on the crystalline-to-amorphous phase transition in PCM is critical for designing low-power nonvolatile memory devices. Therefore, it is desirable to visualize and characterize the critical events that lead to the phase-change process while the device is under operation, which can uncover phenomena that cannot be gleaned from ex situ measurements (*3*). However, it is challenging to resolve the amorphization phenomena with high spatial and/or temporal resolution in confined structures such as in conventional thin-film devices with a sandwich geometry (*4*). Very recently, based on time-resolved photo-excitation measurements of PCM materials (*5*, *6*), it has been argued that the material did not amorphize via the liquid-state pathway, but by a solid-state, lattice-distortion–triggered process. Consequently, visualization of the structural evolution of the PCM device under electrical biasing by correlating it to the electrical-resistance variation would be helpful. A single-crystalline device can serve as an ideal platform to study the relationship between microstructural evolution and electrical resistance variation, so as to avoid the effects of preexisting grain boundaries on carrier transport and structural dynamics. In conventional PCM devices, polycrystalline thin films with relatively small grain sizes (10 to 20 nm) preclude the visualization of switching behavior originating from single grains. By using the single-crystalline, lateral, and open geometry of the $Ge_2Sb_2Te_5$ (GST) nanowire structure, we visualized the amorphization behavior and found it to be critically associated with the nucleation and dynamics of dislocations.

We assembled GST nanowire memory devices across 2-μm-wide trenches fabricated on a thin silicon-nitride membrane (Fig. 1A) to enable real-time visualization of nanoscale structural changes with high spatial resolution under the influence of applied electrical voltage pulses inside a transmission electron microscope (TEM) (figs. S1 to S4) (*7*). Single-crystalline GST nanowires with hexagonal crystal structure grown along the $[10\bar{1}0]$ axis were synthesized through the vapor-liquid-solid method (fig. S1) (*8*). For device operation, voltage pulses with duration of a few hundred nanoseconds were applied, and between each pulse, the resistance was measured at a DC bias of 0.2 V (Fig. 1B). We note that all the reported electrical resistances in this paper are not the dynamic resistances during electrical pulsing, but the stationary resistance values of the devices measured long after the pulsing process so that the heat generated during the pulsing was dissipated and the devices reached room temperature. The resistance (after each 300-ns pulse with increasing voltage amplitude)

[1]Department of Materials Science and Engineering, University of Pennsylvania, Philadelphia, PA 19104, USA. [2]Department of Nuclear Science and Engineering and Department of Materials Science and Engineering, Massachusetts Institute of Technology, Cambridge, MA 02139, USA. [3]Department of Physics and Astronomy, University of Pennsylvania, Philadelphia, PA 19104, USA.

*These authors contributed equally to this work.
†To whom correspondence should be addressed. E-mail: riteshag@seas.upenn.edu

of a 280-nm-thick GST nanowire device as a function of the pulse amplitude (Fig. 1C, blue squares) decreases slightly above 3.3 V, just before amorphization electrical switching was observed. The resistance dip, however, was very small as compared with the more than two orders of magnitude increase in the electrical resistance associated with amorphization switching. There are some critical observations related to the resistance dip: (i) The decrease in the electrical resistance reflects a permanent structural change in the device while still in the crystalline state; and (ii) the critical voltage at which the resistance starts to decrease is a function of the nanowire thickness and pulse width (Fig. 1C and fig. S5). The voltage at which the resistance dip initiates decreased with increasing pulse width, and thicker wires required higher voltages and longer pulses (Fig. 1C, inset).

To correlate the onset of the resistance dip and amorphization with structural evolution, we show snapshots of the dark-field (DF) TEM movie (movie S1) and the corresponding electrical resistances of a nanowire device in Fig. 2. The resistance dip before amorphization was a general feature of all nanowire devices measured either inside or outside the TEM. For a 230-nm nanowire device, no structural changes in the DF TEM images were identified until ~5 V pulses (800 ns), but concomitant with the onset of the resistance dip, the uniform contrast of the single-crystalline device started to change dynamically, with extended line-shaped defects (Fig. 2B) and other strain-related contrasts. For voltages below the resistance dip (<5.8 V), the contrast continued to change upon each applied pulse, but no directional motion was observed. High-resolution TEM characterization of the line defects reveals the presence of dislocations (fig. S6) with a Burgers vector of $\frac{1}{3}\langle 11\bar{2}0\rangle$. Considering the hexagonal-crystalline structure of GST grown along the $[10\bar{1}0]$ axis, the line-shape structure represents the projection image of the dislocation loop that lies on the $(10\bar{1}0)$ prismatic plane, as illustrated in Fig. 1A.

Notably, upon further increasing the voltage pulse amplitude (800 ns duration), the resistance dip was directly associated with the line defects becoming mobile and propagating along the direction of hole-carrier motion (Fig. 2, C to F). This observation suggests the influence of the carrier wind force to break the symmetry of the nanowire for dislocation motion, thereby inducing a polarity-dependent behavior (*9*–*11*). The resistance continued to drop with the increase in the pulse amplitude, accompanied with the motion of dislocations from the positive to the negative electrode. In particular, dynamic contrast changes were observed moving unidirectionally in the device. Upon approaching the bottom of the resistance dip, it was observed that the dislocations stopped moving (jamming), followed by the formation of highly accumulated and entangled dislocations at the jammed location (Fig. 2, G and H, and movie S1). Finally, amorphization switching was observed, accompanied by an increase in the electrical resistance by approximately two orders of magnitude. A clear bright line was identified as the amorphous phase (red arrow, Fig. 2I), which was further characterized by electron diffraction studies (fig. S7). TEM image of the free-standing region of the nanowire (over the trench) in Fig. 2J shows a trail of dislocation cloud right behind the amorphized region. In addition, a few other dislocation cloud trails were identified along the nanowire but without any amorphous marks, which indicates that they got jammed by random perturbation in the nanowire structure, with one among them eventually undergoing amorphization. These observations show that the entangled dislocations

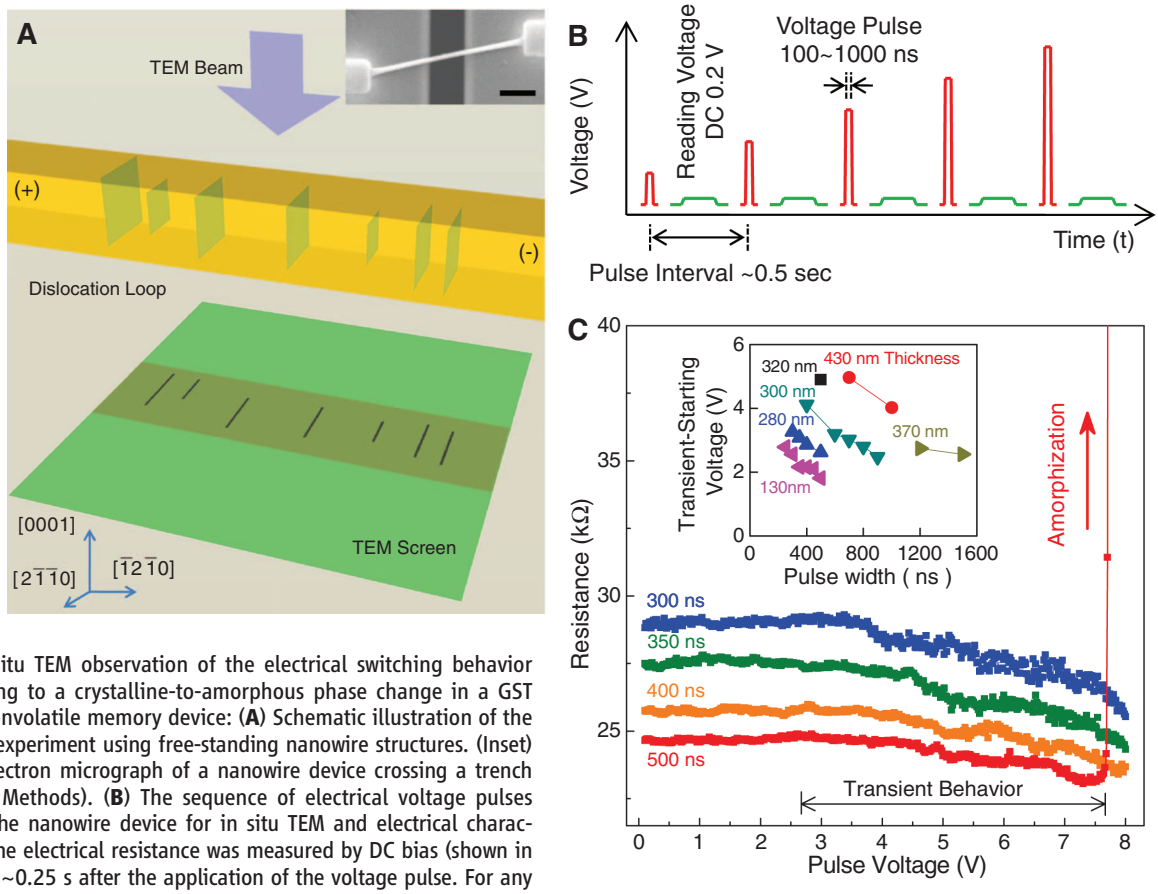

Fig. 1. In situ TEM observation of the electrical switching behavior corresponding to a crystalline-to-amorphous phase change in a GST nanowire nonvolatile memory device: (**A**) Schematic illustration of the in situ TEM experiment using free-standing nanowire structures. (Inset) Scanning electron micrograph of a nanowire device crossing a trench region (see Methods). (**B**) The sequence of electrical voltage pulses applied to the nanowire device for in situ TEM and electrical characterization. The electrical resistance was measured by DC bias (shown in green) after ~0.25 s after the application of the voltage pulse. For any pulse sequence, the amplitude of the applied voltage pulse was increased with a 0.5-s interval between any two pulses while their widths were kept constant. (**C**) Plots of electrical resistance of the nanowire device versus applied voltage pulse amplitude obtained for different pulse width sequences, starting from a single-crystalline state. Resistance dip was observed before amorphization switching. (Inset) A plot of nanowire size versus the voltage at which the resistance dip is initiated as a function applied pulse widths.

caused by dislocation generation and jamming are precursors for the amorphization switching of the device.

To confirm that the electrical polarity determines the direction of propagation of dislocations by the carrier wind force, we performed a "reverse-bias" experiment with the opposite polarity applied on the same device (Fig. 2, K to T, and movie S2). The device was first switched back to the crystalline state, followed by the continuous application of electrical pulses with the opposite polarity in the same sequence as described above. Upon applying 500-ns-width pulses, the resistance dip was observed, during which the jammed dislocation cloud from the previous measurement was relieved by moving in the opposite direction. We then stopped pulsing at 5 V, and then applied 800-ns pulses starting from 0 V. The device resistance started from the resistance at which we stopped the 500-ns pulses (Fig. 2K), which then began to dip again from ~2 V (longer pulses lead to onset of resistance dip at lower voltages). Dynamic contrast changes were observed to move in the opposite direction, which again corresponds to the direction of the hole carriers (movie S2). Eventually, amorphization switching occurred at ~5.2 V (Fig. 2, P to S), with the dislocation cloud appearing behind the amorphous mark, consistent with the forward-bias experiments (Fig. 2T). The reverse-bias pulsing experiment clearly indicates that the mobile dislocations are transported in the direction of the applied bias, which is the direction of the motion of hole carriers in the device, suggesting a critical role of dislocation nucleation, motion, and jamming in creating the amorphous phase in the PCM device.

To better visualize the amorphization switching process, we sculpted a notch structure in the nanowire suspended over the trench to localize the phase-change region at the notch (Fig. 3) (*3*). In bright-field (BF) TEM image, the as-fabricated nanowire appeared uniformly dark owing to its single crystallinity (Fig. 3A). During electrical pulsing (movie S3), a change in the

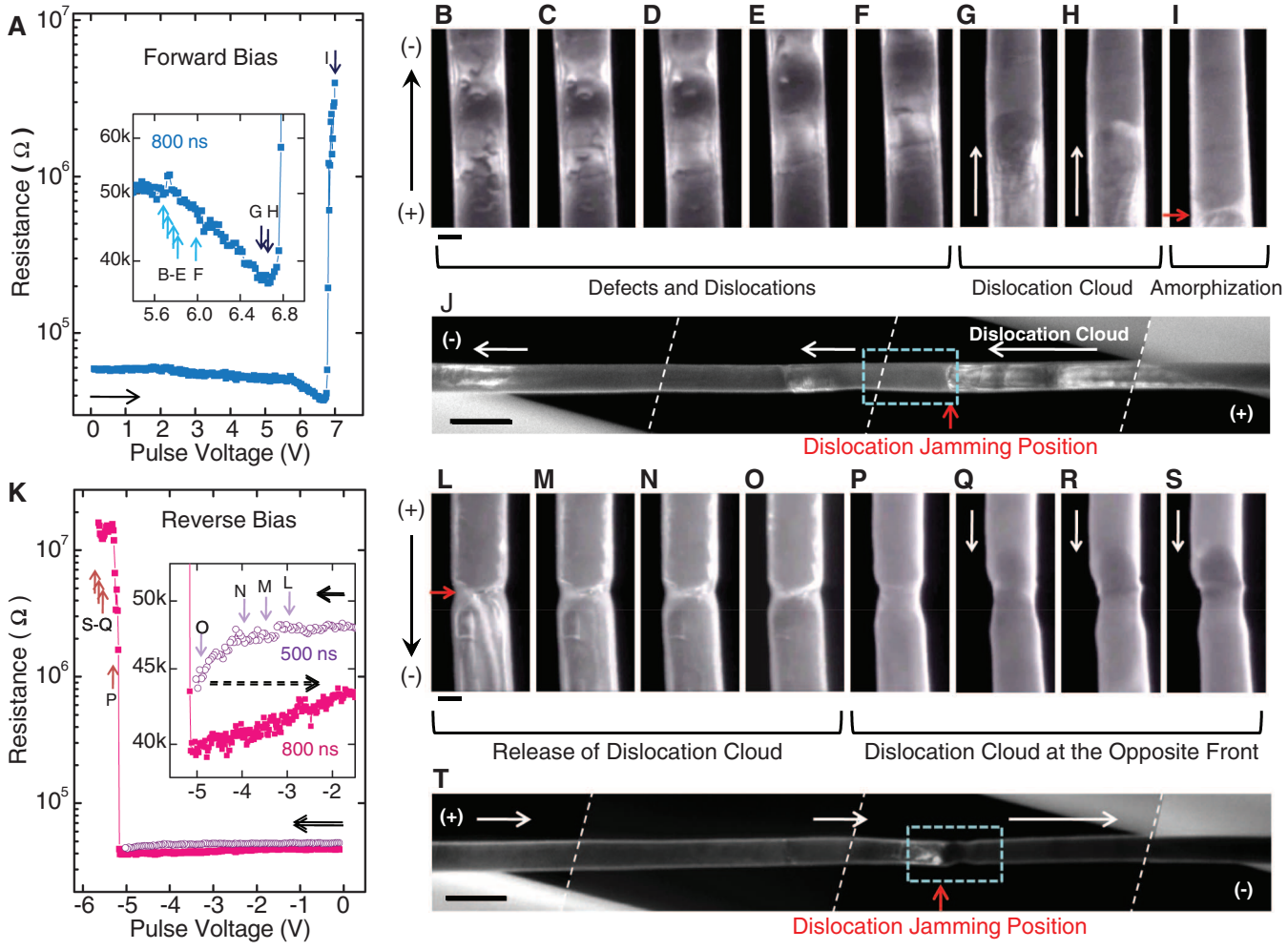

Fig. 2. Electric wind force–driven mobile dislocations and amorphization switching via in situ TEM measurements: (**A** to **J**) "Forward-bias"; (**K** to **T**) "reverse-bias," i.e., opposite polarity from the same region of the device. (A) Plot of stationary electrical resistance of the nanowire device versus voltage pulse amplitude for the forward-bias direction. The electrical resistance states are correlated with the TEM images of the device, as indicated by arrows. (B to I) Snapshots of DF TEM images (from movie S1) during electrical switching: At the early stage, individual dislocations were identified in (B) to (E), which started to propagate along the hole-carrier motion direction (F to I). The white arrows indicate the unidirectional motion of the TEM image contrast. At the bottom of the electrical resistance dip, a dislocation cloud was observed in (G) and (H). Following the resistance dip regime, amorphization occurred at the dislocation jamming region [red arrow in (I)]. (J) Larger-area DF TEM image of the free-standing GST nanowire device after amorphization, showing a dislocation trail behind the amorphized region. The blue rectangular area was recorded in the TEM movie (movie S1). (K) Plot of electrical resistance versus voltage pulse amplitude for the reverse-bias case. (L to S) From movie S2; the dislocation cloud behind the jamming region was first relieved (L to O), and subsequently another dislocation cloud was developed on the opposite front of the jamming transition region (P to S). (T) Larger-area DF TEM image of the nanowire after the reverse-polarity–biased amorphization switching, again showing a dislocation trail behind the amorphized region, but in the opposite direction as compared with (J). Scale bar: (B to I) and (L to S), 100 nm; (J and T), 500 nm. The dashed lines in (J) and (T) denote the regions where the images were combined.

image contrast was observed while the device was still in the crystalline state, with the notch region developing a dark line contrast (Fig. 3B), followed by a contrast variation moving from the positive- to the negative-electrode side (Fig. 3C). The image contrast variation along the nanowire was again correlated with the resistance dip, consistent with our previous observations for the non-notched devices. Finally, upon amorphization switching, the dark line in the middle of the notch was abruptly changed into a bright amorphous band (Fig. 3D). Microstructure analysis (BF TEM images) both before and after the switching (fig. S8) shows that a highly strained structure developed in the notch region before amorphization. In particular, the amorphous mark appeared in this region of strain, which suggests the role of strain in the amorphization process. The origin of the strained structure and the differential contrast was further studied by DF TEM analysis (Fig. 3E). DF TEM revealed the presence of a high density of dislocations, predominantly at the positive-electrode side of the notch (Fig. 3E). Even though the notch structure was intended to localize joule heating by enhancing the current density, our in situ observation additionally suggests that the notch was also more likely to behave as a geometrical necking region where mobile dislocations were jammed and accumulated by the electrical wind force that did not pass through the constriction easily (see also fig. S9 for results from another device).

In contrast to thin-film polycrystalline GST, which consists of small grains (10 to 20 nm), the single-crystalline nanowire structure rules out the effect of preexisting grain boundaries for both structural evolution and resistance dip. Our observations show that the dislocations are continuously nucleated along the single-crystalline GST nanowire, which become mobile above a certain applied voltage that is correlated to the resistance dip. The voltage pulses play a critical role by inducing heat shocks along the single-crystalline nanowire, which create dislocations by vacancy condensation (*12*). The rising edge of the pulse produces lattice vacancies in the material caused by heating, with the nanowire surface/interface serving as the lattice vacancy source, whereas during rapid cooling, atomic vacancies are condensed into dislocation loops by nonconservative dislocation climb (*12*, *13*) (fig. S10). This mass-action dislocation generation path is different from purely displacive shear nucleation driven by an external mechanical stress (*14*–*18*). Because our nanowire is a free-standing structure where the thermal-expansion stress is relieved from its surface (*19*) and by buckling, the dislocation formation is attributed more to vacancy supersaturation (osmotic forces) than to mechanical stress. After formation, these dislocations feel the directional electrical wind force, but display a threshold behavior in mobility: that is, as a whole, they only start to move when the electrical wind force exceeds a critical value. When the dislocations become mobile, they consume more vacancies along the way by combined climb and glide actions, which decrease the carrier scattering probability, thereby decreasing the electrical resistance of the device (Fig. 1C) (*13*). (Dislocation dynamics are illustrated in figures S11 to S14.) Similar electrical resistance drops have been observed during rapid annealing of metals, attributed to Frank and prismatic dislocation loop nucleation and growth driven by vacancy condensation (*13*). Therefore, we believe that an electrical current pulse has two physical effects, one directional and the other nondirectional. The nondirectional thermal heating and quenching produce the dislocations, whereas the directional wind force moves the dislocations in the drift direction of the majority charge carrier (holes in the case of GST), leading to polarity dependence. Yang *et al*. (*10*) have reported that hole-carrier wind force in GST induces a mass transport by electromigration at high current densities, which partly corroborates our observation of polarity-dependent dislocation motion.

One question that arises naturally is, what specific properties of GST lead to the observation of dislocation nucleation and transport, which is quite different from those in other covalently bonded materials such as silicon? To understand dislocation transport in crystalline hexagonal GST, we performed ab initio density functional theory (DFT) calculations to characterize slip systems of a prismatic dislocation loop. The DFT calculations for basal $(0001)[11\bar{2}0]$ and prismatic $(1\bar{1}00)[11\bar{2}0]$ slips exhibit unstable generalized-stacking-fault (GSF, γ) energies of 10.1 and 172.8 mJ/m^2, respectively (Fig. 4A and fig. S15). $\gamma_{\text{unstable}}^{(0001)[11\bar{2}0]}$ is extremely small [similar to basal slip in graphite (*20*)]; in GST-layered structures with

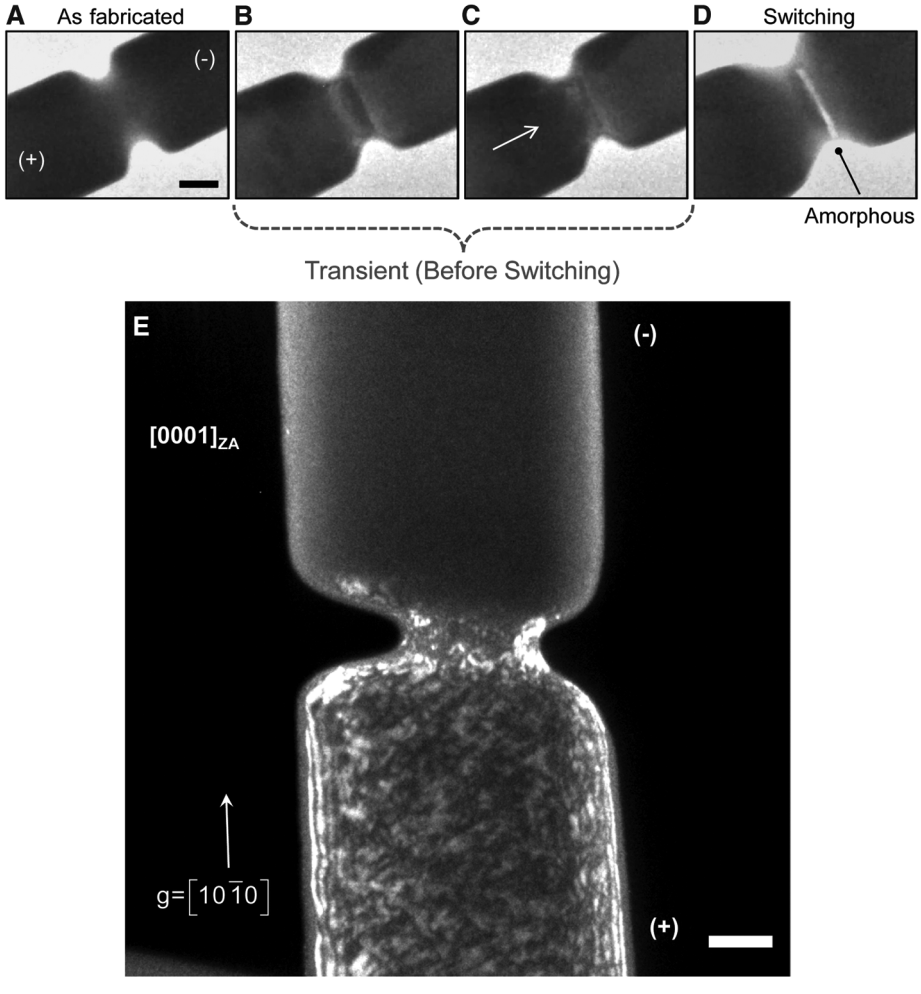

Fig. 3. Transient behavior (region of resistance dip) followed by amorphization switching for a nanowire device with a notch (constriction). (**A** to **D**) Snapshots from BF TEM movie (movie S3): As-fabricated nanowire device shows a uniform, dark contrast along the nanowire in (A). As the electrical pulses were applied, the variation in TEM image contrast was identified at the moment of the initiation of the resistance dip. Darker line in the middle of the notch in (B) and (C) shows a region of highly concentrated strain, which was changed into bright contrast upon amorphization (D). (**E**) DF TEM image of the single-crystalline nanowire close to the bottom of the transient resistance dip: A dislocation cloud was located mostly at the (+) electrode region in (E). Scale bars (A and E), 100 nm.

a stacking sequence -Sb-Te-Ge-Te-Te-Ge-Te-Sb-Te- (also occurs in cubic GST) (*21*), weak Te-Te bonding on the basal plane is the most likely to slip because of its long bond length and weak bonding energy (*22*). $\gamma_{unstable}^{(1\bar{1}00)[11\bar{2}0]}$ is quite small also, comparable to that for partial dislocation slip in Cu (169 mJ/m^2) (*23*), and much smaller than those for slips in Si (>1500 mJ/m^2) (*24*); thus, motion of prismatic dislocation loops driven by the electrical wind force is feasible in GST (for crystallographic details on glide of prismatic loops, refer to figs. S11 to S14).

We summarize the dislocation generation and dynamics leading to amorphization switching in Fig. 4B. Both heat (nondirectional) and carrier wind force (directional) effects are consequences of the applied voltage pulses. Just before the initiation of the resistance dip, the heat-shock process by the electrical pulses leads to generation of vacancies followed by their rapid condensation to generate dislocations, analogous to generation of Frank-partial and prismatic dislocations in face-centered cubic metals by vacancy condensation (*25*). From our observation, it is likely that most of the dislocations are generated at the positive-bias metal electrode in contact with the nanowire (owing to material incompatibility and larger potential drop), but some of them can also be generated along the nanowire. As the amplitude of voltage pulses increases, the carrier wind force makes the dislocations mobile, gliding as prismatic dislocation loops. These dislocation loops grow in size as they move, encounter, and annihilate more vacancies, acting as "garbage collectors," which decrease the total disorder in the crystal, but also transport some disorder (in the form of dislocation cores) downstream in a one-dimensional (1D) traffic flow along the nanowire.

One-dimensional traffic flows are inherently fragile and prone to instabilities, because of interactions between the mobile agents that lead to density-dependent mobility (*26*). For instance, analytical models of automobile traffic on a highway predict sharp, catastrophic jamming when the automobile density exceeds a certain fraction of the maximum packing density (*27*). Owing to the mutual tangling that lowers their 1D mobility, the mobile dislocations moving in the direction of the hole drift can jam at some location. The dislocations then accumulate at the jammed region of the nanowire, which creates a high degree of disorder locally in the crystalline material, leading eventually to amorphization switching (*28*–*31*). Therefore, paradoxically, the mobile extended defects, which decrease the crystalline disorder elsewhere, can also greatly concentrate the disorder in a local region, when the jamming transition occurs. For nanowires without a notch, the dislocation jamming can occur anywhere when a critical dislocation density is reached in the system.

Our observations show that amorphization in PCM devices is templated by dislocation transport and jamming in the crystal. If the devices were amorphized by conventional melt-quench process, then one would have expected initiation of melting from the nanowire surface that should have spread, eventually leading to an amorphous shell around a crystalline core. Such a mechanism would have led to poor on/off resistance ratios because of resistors in parallel. In contrast, we have always observed the amorphous phase form in series with the crystalline phase (*3*), with the amorphous volume occupying just a tiny fraction of the total device volume, yet achieving good device performance with large on/off resistance ratios. Furthermore, in all the measured devices, the amorphous mark always appeared in front of the jammed dislocation cloud spanning the entire cross section of the nanowire and with very sharp vertical interfaces, with no amorphous phase seen anywhere else. It is thus evident that the dislocation jam with vertical boundaries provides a microstructural template for amorphization to occur in a vertical section, which is different from conventional understanding of melting that is templated by free surfaces. Solid-state amorphization is known to occur in silicon (*29*) and metallic (*31*) crystals by mechanical ball milling that injects a high density of dislocations into the material, where melting is not possible at room temperature. We cannot completely rule out the possibility of transient melting in the dislocated region, because dislocations do increase the local resistance and heat generation. The physics of such atomic disordering around dislocation cores—i.e., premelting (*32*)—even if it occurs, would be quite different from normal melting, because the degree of atomic disordering around dislocation cores can only rise gradually with temperature, unlike a sharp first-order thermodynamic transition in a conventional bulk melting process. In any case, our main result, which is dislocation-templated amorphization of narrow cross section with a sharp interface, is microstructural—independent of the detailed chemical physics of atomic disordering—and consistent with the observed device performance (large on/off ratio). Our results, based on direct observation by in situ TEM analysis, are consistent with several recent reports (*5*, *6*, *33*) that also have suggested non- (conventional) melting–based amorphization process in GST material.

The observation of the voltage pulse–induced dislocation nucleation, wind force–assisted dislocation glide and jamming, and subsequent dislocation-templated amorphization shed light on previously unexplored properties of these fascinating materials, relating microstructural evolution to device properties. A similar mechanism could operate in polycrystalline thin-film devices as the grain boundaries can be considered as networks of dislocations and also act as dislocation sources and sinks. Furthermore, direct visualization of various processes occurring in PCM devices under electrical bias would be promising to understand their unusual fast switching behavior and will also be applicable to other functional materials and devices.

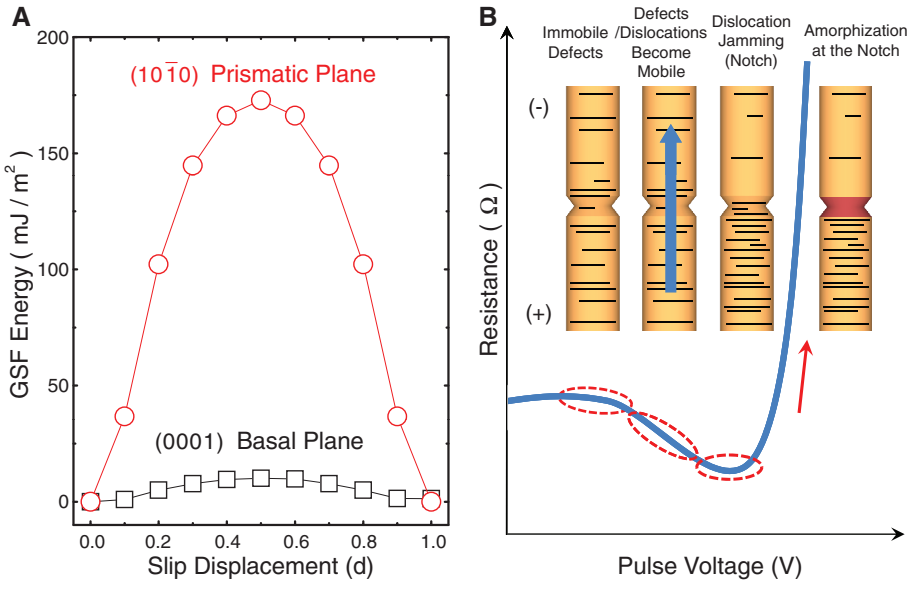

Fig. 4. (**A**) DFT calculation of generalized stacking fault (GSF) energy for both basal (0001) and prismatic (10$\bar{1}$0) planes in hexagonal $Ge_2Sb_2Te_5$. (**B**) Our model of dislocation nucleation, transport, and jamming by electrical pulses: At the initiation of the dip of electrical resistance, the electrical pulses induce heat shocks to nucleate dislocations from atomic vacancies. As the pulse voltage amplitude increases, the dislocations become mobile and move along the direction of holes owing to the carrier wind force. Eventually, because of the increase in dislocation density, there is a jamming transition (e.g., in the notch region or elsewhere for regular wires), where the dislocations pile up, followed by amorphous switching in the same region. On the other side of the notch, the dislocations move away from the observed region in TEM owing to wind force.

References and Notes

1. M. Wuttig, N. Yamada, *Nat. Mater.* **6**, 824 (2007).
2. S. Raoux, *Annu. Rev. Mater. Res.* **39**, 25 (2009).
3. Y. Jung, S. W. Nam, R. Agarwal, *Nano Lett.* **11**, 1364 (2011).
4. B. J. Kooi, W. M. G. Groot, J. T. M. De Hosson, *J. Appl. Phys.* **95**, 924 (2004).
5. P. Fons *et al.*, *Phys. Rev. B* **82**, 041203(R) (2010).
6. A. V. Kolobov, M. Krbal, P. Fons, J. Tominaga, T. Uruga, *Nat. Chem.* **3**, 311 (2011).
7. D. R. Strachan *et al.*, *Phys. Rev. Lett.* **100**, 056805 (2008).
8. S. H. Lee, Y. Jung, R. Agarwal, *Nat. Nanotechnol.* **2**, 626 (2007).
9. S. W. Nam *et al.*, *Electrochem. Solid-State Lett.* **12**, H155 (2009).
10. T. Y. Yang, I. M. Park, B. J. Kim, Y. C. Joo, *Appl. Phys. Lett.* **95**, 032104 (2009).
11. M. H. Lee *et al.*, *IEEE International Electron Devices Meeting (IEDM)*, 28.6.1. (2010).
12. G. Schoeck, W. A. Tiller, *Philos. Mag.* **5**, 43 (1960).
13. H. Kimura, R. Maddin, D. Kuhlmannwilsdorf, *Acta Metall.* **7**, 145 (1959).
14. H. Zheng *et al.*, *Nat. Commun.* **1**, 144 (2010).
15. Z. W. Shan, R. K. Mishra, S. A. Syed Asif, O. L. Warren, A. M. Minor, *Nat. Mater.* **7**, 115 (2008).
16. S. H. Oh, M. Legros, D. Kiener, G. Dehm, *Nat. Mater.* **8**, 95 (2009).
17. Q. Yu *et al.*, *Nature* **463**, 335 (2010).
18. T. Zhu, J. Li, A. Samanta, A. Leach, K. Gall, *Phys. Rev. Lett.* **100**, 025502 (2008).
19. M. Mitra, Y. Jung, D. S. Gianola, R. Agarwal, *Appl. Phys. Lett.* **96**, 222111 (2010).
20. R. H. Telling, M. I. Heggie, *Philos. Mag. Lett.* **83**, 411 (2003).
21. A. V. Kolobov *et al.*, *Nat. Mater.* **3**, 703 (2004).
22. Z. M. Sun, J. Zhou, R. Ahuja, *Phys. Rev. Lett.* **96**, 055507 (2006).
23. S. Ogata, J. Li, S. Yip, *Phys. Rev. B* **71**, 224102 (2005).
24. E. Kaxiras, M. S. Duesbery, *Phys. Rev. Lett.* **70**, 3752 (1993).
25. D. Hull, D. J. Bacon, *Introduction to Dislocations* (Butterworth-Heinemann, Oxford, ed. 4, 2001).
26. K. Nagel, *Phys. Rev. E Stat. Phys. Plasmas Fluids Relat. Interdiscip. Topics* **53**, 4655 (1996).
27. D. Helbing, *Rev. Mod. Phys.* **73**, 1067 (2001).
28. D. Wolf, P. R. Okamoto, S. Yip, J. F. Lutsko, M. Kluge, *J. Mater. Res.* **5**, 286 (1990).
29. J. Y. Huang, H. Yasuda, H. Mori, *Philos. Mag. Lett.* **79**, 305 (1999).
30. J. Y. Huang *et al.*, *Science* **330**, 1515 (2010).
31. J. Y. Huang, Y. T. Zhu, X. Z. Liao, R. Z. Valiev, *Philos. Mag. Lett.* **84**, 183 (2004).
32. Y. Mishin, M. Asta, J. Li, *Acta Mater.* **58**, 1117 (2010).
33. A. V. Kolobov *et al.*, *Phys. Rev. Lett.* **97**, 035701 (2006).

Acknowledgments: This work was supported by the Office of Naval Research (grant N000140910116), Materials Structures and Devices Center at the Massachusetts Institute of Technology, NSF (DMR-0706381 and DMR-1002164), and Penn-Materials Research Science and Engineering Center (DMR05-20020 and DMR11-20901). Y.C.L., L.Q., and J.L. acknowledge the support of NSF DMR-1008104 and DMR-1120901, and Air Force Office of Scientific Research FA9550-08-1-0325. Y.L. and A.T.C.J. acknowledge the support of the Nano/Bio Interface Center through NSF Nanoscale Science and Engineering Center DMR08-32802. Electron microscopy experiments were performed at the Penn Regional Nanotechnology Facility at the University of Pennsylvania. S.-W.N. thanks D. Strachan for useful discussions on in situ TEM experiments. The data described in the paper are archived by the Agarwal group at the University of Pennsylvania.

Supplementary Materials

www.sciencemag.org/cgi/content/full/336/6088/1561/DC1
Materials and Methods
Figs. S1 to S15
References
Movies S1 to S3

6 February 2012; accepted 18 May 2012
10.1126/science.1220119

Breaking the Speed Limits of Phase-Change Memory

D. Loke,[1,2,3]* T. H. Lee,[2]* W. J. Wang,[1] L. P. Shi,[1]† R. Zhao,[1] Y. C. Yeo,[4] T. C. Chong,[5] S. R. Elliott[2]†

Phase-change random-access memory (PCRAM) is one of the leading candidates for next-generation data-storage devices, but the trade-off between crystallization (writing) speed and amorphous-phase stability (data retention) presents a key challenge. We control the crystallization kinetics of a phase-change material by applying a constant low voltage via prestructural ordering (incubation) effects. A crystallization speed of 500 picoseconds was achieved, as well as high-speed reversible switching using 500-picosecond pulses. Ab initio molecular dynamics simulations reveal the phase-change kinetics in PCRAM devices and the structural origin of the incubation-assisted increase in crystallization speed. This paves the way for achieving a broadly applicable memory device, capable of nonvolatile operations beyond gigahertz data-transfer rates.

Phase-change random-access memory (PCRAM) represents one of the best candidates for a so-called "universal memory" due to its nonvolatile nature, high scalability, low power consumption, high read/write speeds, and long read/write endurance (*1*–*4*). PCRAM operations, based on the reversible switching of phase-change (PC) materials between amorphous and crystalline states (*5*, *6*), are generally fast: on the order of nanosecond time scales (*7*–*9*). However, the crystallization speed is much slower than the amorphization speed, which limits the overall writing speed of PCRAMs. Despite efforts (*10*–*16*) to increase the crystallization speed, it has been difficult to achieve a speed faster than 1 ns. A difficulty arises from the contradictory nature of increasing the crystallization speed while extending the stability of PC materials for long-term data retention (*17*). This has restricted the selection of PC materials in the commercial development of PCRAMs, typically emphasizing high stability at the expense of crystallization speeds.

According to classical nucleation theory, the nucleation of small crystallites and their subsequent growth are the two main distinct processes in crystallization (*18*–*20*). The nucleation rate is faster at lower temperatures, followed by rapid growth at higher temperatures (*21*). We show that by stimulating and altering these processes, we are able to control the speed of crystallization by electrical means. Our approach is based on the idea of providing a weak electric field to induce thermal prestructural ordering (incubation of ordered clusters in the amorphous matrix) via Joule heating, which enables faster nucleation and growth upon a subsequent stronger electrical pulse, while maintaining the high stability of the amorphous phase by controlling the cluster-size distribution (Fig. 1). This thermal-incubation model is very different from the model of Karpov *et al.* (*22*), which assumes a direct electric-field–induced modification of the crystal-nucleation barriers in $Ge_2Sb_2Te_5$ (GST).

We experimentally fabricated porelike structured PCRAM cells (with GST as the PC material) and used these cells to study the incubation effects on the crystallization speeds (Fig. 1D) (*23*). To study the ultrafast switching effects, a weak electric field (equivalent to ~0.3 V), for tailoring the crystallization kinetics (hereafter referred to as the incubation field), was employed to achieve optimal switching properties without activating spontaneous crystallization (fig. S2). We employed subsequent electrical pulses (varying in length from several hundred picoseconds to several tens of nanoseconds) to switch the cells, and we used the full width at half maximum (FWHM) values of the pulses to characterize the switching speeds of the cells (fig. S3). The duration of a pulse experienced in the cell was confirmed to be the same as that measured before the pulse enters the cell (fig. S4).

We found that the incubation field, even with the small amount of thermal energy it delivers, can substantially promote the nucleation and growth of PC materials. Nucleation and growth times can be characterized by the minimum electrical pulse width needed to switch the cell from the amorphous state to the crystalline state (*24*), also known as the "set" process. When the incubation field is applied to a cell (Fig. 2A), much faster nucleation and growth are observed, as manifested by the substantial decrease in pulse width (by ~5 ns). For the fastest nucleation and growth, we found the shortest pulse to be 500 ps. This is approximately one order of magnitude

[1]Data Storage Institute, Agency for Science, Technology and Research (A*STAR), 5 Engineering Drive 1, Singapore 117608. [2]Department of Chemistry, University of Cambridge, Lensfield Road, Cambridge CB2 1EW, UK. [3]National University of Singapore (NUS) Graduate School for Integrative Sciences and Engineering, 28 Medical Drive, Singapore 117456. [4]Department of Electrical and Computer Engineering, National University of Singapore, 4 Engineering Drive 3, Singapore 117576. [5]Singapore University of Technology and Design, 20 Dover Drive, Singapore 138682.

*These authors contributed equally to this work.
†To whom correspondence should be addressed. E-mail: shi_luping@dsi.a-star.edu.sg (L.P.S.); sre1@cam.ac.uk (S.R.E.)